LA-UR- 11-05559

Approved for public release;
distribution is unlimited.

Title:	Towards the experimental assessment of NLBeam for modeling large deformation structural dynamics
Author(s):	D. J. Luscher -T-3
Intended for:	IMAC XXX A Conference and Exposition on Siructural Dynamics Jacksonville, FL USA Jan. 30-Feb.2, 2012

Los Alamos
NATIONAL LABORATORY
EST.1943

Los Alamos National Laboratory, an affirmative action/equal opportunity employer, is operated by the Los Alamos National Security, LLC for the National Nuclear Security Administration of the U.S. Department of Energy under contract DE-AC52-06NA25396. By acceptance of this article, the publisher recognizes that the U.S. Government retains a nonexclusive, royalty-free license to publish or reproduce the published form of this contribution, or to allow others to do so, for U.S. Government purposes. Los Alamos National Laboratory requests that the publisher identify this article as work performed under the auspices of the U.S. Department of Energy. Los Alamos National Laboratory strongly supports academic freedom and a researcher's right to publish; as an institution, however, the Laboratory does not endorse the viewpoint of a publication or guarantee its technical correctness.

Form 836 (7/06)

Towards the experimental assessment of *NLBeam* for modeling large deformation structural dynamics

Sarah Dalton[1], Lisa Monahan[2], Ian Stevenson[3], D.J. Luscher[4*], Gyuhae Park[4], Kevin Farinholt[4]

[1]Clemson University, Clemson, SC 29634
[2]University of Pittsburgh, Pittsburgh, PA 15260
[3]Rose-Hulman Institute of Technology, Terre Haute, IN 47803
[4]Los Alamos National Laboratory, Los Alamos, NM 87545

Abstract

With the growth of the wind energy industry, it has become apparent that gear boxes in wind turbines, which link the blades to the generator, tend to wear down faster than anticipated. This phenomenon is not clearly understood; one theory is that existing wind turbine modeling approaches used to design the turbines do not properly account for nonlinearities caused by large amplitude blade deformations. To help understand the effects of geometric nonlinearities, a finite element based code, *NLBeam*, has been developed to simulate structural dynamic responses of wind turbine blades by employing the geometrically exact beam theory. This research focuses on assessing the adequacy of *NLBeam* by comparing simulation to experimental results. Three aluminum blade surrogates with different geometries were tested by applying large amplitude base excitations while assuring the surrogates stayed within the elastic range. A variety of orientations were utilized changing the dynamic characteristics of the surrogates and reflecting actual turbine blade behavior. The results are used to guide future development of *NLBeam* which will be coupled with large scale simulations of wind plants in a Computational Fluid Dynamics based program developed at Los Alamos National Laboratory called *WindBlade*.

1. Introduction

In a 2008 report published by the Department of Energy, the possibility of providing 20 percent of the United States' power supply through wind energy by 2030 was assessed [1]. To accomplish such a feat, it is projected that wind energy production must increase beyond 300 gigawatts (GW) by 2030, an increase of 25 orders of magnitude in 23 years. In order to meet this increase in energy demand, wind plants are expanding in size and requiring the optimization of turbine placement to most efficiently produce power for a given wind input. Concurrently, individual wind turbines are manufactured larger and with higher capacities. Turbine blade lengths are continually increasing in order to more efficiently extract power from wind, however, a corresponding increase in displacement and, even more importantly, large magnitudes of rotation associated with deformation also occur. Such deformations, for example, blade torsion, influence angle-of-attack and ultimately affect wind flow at the plant scale in a coupled manner. To model the wind and turbine-turbine interactions at a plant scale, Los Alamos National Laboratory has developed a computational fluid dynamics (CFD)-based wind plant simulation code called *WindBlade* [2].

To realize such production, it is imperative that wind power production not only increase in capacity, but also become more economically viable. A clear area to reduce wind energy costs is to increase wind turbine reliability. Wind turbines include multiple assemblages which interact and transfer loads to the foundation. Evidence has been found indicating certain assemblies, such as the gearbox, are plagued by premature failures [3]. The cause is not clearly understood; one theory is that existing wind turbine modeling approaches do not properly account for nonlinearities caused by large amplitude blade deformations. Consequently, the actual loads transmitted through the wind turbine blades are higher than anticipated.

*Email correspondence to: djl@lanl.gov

With the growing desire to harvest wind power at increased demand levels, the length of turbine blades and the number of turbines erected in wind plants is ever increasing. Modeling these plants to determine the most efficient layout is difficult due to the complex nature of aerodynamic loading on turbines, mainly due to variable inflow conditions as shown by Robinson et al. [4]. The deeper the wind penetrates into the plant, the more turbines it interacts with, creating noise effects on the wind flow. The noisy wind conditions imposed upon downwind turbines complicate both the modeling of structural loading on the turbines and the modeling of their ability to capture energy [5]. LANL's *WindBlade* aims to model the interactions of wind and turbines [2]; however, it currently assumes rigid body dynamical motion of the turbine rotors. This simplification does not account for the change in angle of attack with respect to the wind when blades deform and rotate. Furthermore, the actual loads being transmitted throughout the wind turbine system are not computed, thus losing available insight on the influence of the dynamic wind field on the structural loading. Essentially, key aspects of the aeroelastic interaction between the wind and wind turbines are not captured. To improve this plant scale simulation capability, a more complete representation of wind turbine structural dynamics must be implemented into *WindBlade*.

One such approach has been developed by the National Renewable Energy Laboratory (NREL) leading to the implementation of a code coined FAST (Fatigue, Aerodynamics, Structures, and Turbulence) [6,7]. FAST utilizes equations of motion for the modeling of complex dynamic systems derived from Kane's method. This theory differs from other methods for obtaining equations of motion such as Lagrange's method, D'Alembert's method, and Newton-Euler's method, in that Kane's method parameterizes the motion of deformation into decoupled orthogonal modes [8, 9]. In order to model flexible elements, FAST utilizes linear modal characterization assuming small deformations [7]. This approach can be inauspicious in that (i) the small deformation assumption is often not held; inducing geometric nonlinearities and (ii) the reliability of the model depends on the validity of mode shapes over a range of operating conditions which are input into FAST from a separate code [6].

Another approach is to develop detailed, high fidelity three-dimensional finite element (FE) models to couple with the fluid-structure interactions of wind turbine blades [10-12]. These high fidelity models are advantageous in modeling both the spatial and temporal multi-scale physics to be accurately modeled throughout the entire system over a given time period. However, the computational costs associated with running simulations of this level of sophistication preclude application at the plant scale as accomplished by *WindBlade*.

An alternative approach, as employed in this paper, strikes a balance between accurately representing generally nonlinear behavior with the computational costs when considered as an integral part of a plant-scale simulation code. In particular, this research uses the geometrically exact beam theory such as developed by Reissner [13,14], Simo [15], Simo and Vu-Quoc [16], Jelenic and Crisfield [17], for example. The use of this method is advantageous in comparison to those modeling techniques of rigid body systems, linear modal representations, or high fidelity modeling due to its ability to handle the nonlinear problem in a computationally efficient manner [17,18]. In the context of this paper, it is important to note that *geometrically exact* implies the treatment of finite rotation of each cross section as exact, obviating any small-angle approximations [19]. The geometrically exact beam theory exploits the slenderness of beams, allowing for dimensional reduction, i.e., the simplification of a geometrically nonlinear 3D problem by decoupling the problem into a linear 2D cross-sectional analysis and a nonlinear beam problem along a reference axis [19]. This approach preserves geometric nonlinearities in a computationally tractable manner when representing beam deformations [17-19].

A finite element code, *NLBeam*, was developed to implement this theory for application to modeling coupled fluid-structure dynamics within *WindBlade*. The research presented in this paper aims to initiate validation of that code by (1) developing an experimental methodology to isolate geometric nonlinearity in structural dynamics of flexible beams, and (2) assess the predictive modeling capabilities of *NLBeam* in capturing large amplitude blade dynamics by comparing experimental results with *NLBeam* simulations for dynamically driven surrogate blades. Moreover, a secondary objective aims to contribute to a body of evidence which can be used to aid in the future development and validation of *NLBeam*.

2. Geometrically Exact Beam Theory

NLBeam employs the geometrically exact beam theory to represent the geometric nonlinearity associated with generally large rotations. Geometrically exact beam theory dates back to the pioneering work of Reissner and Simo and Vu_Qouc and has been extensively developed over the last three decades [14-19] and applied, for example, to helicopter rotor dynamics [18]. The theory is only briefly summarized here.

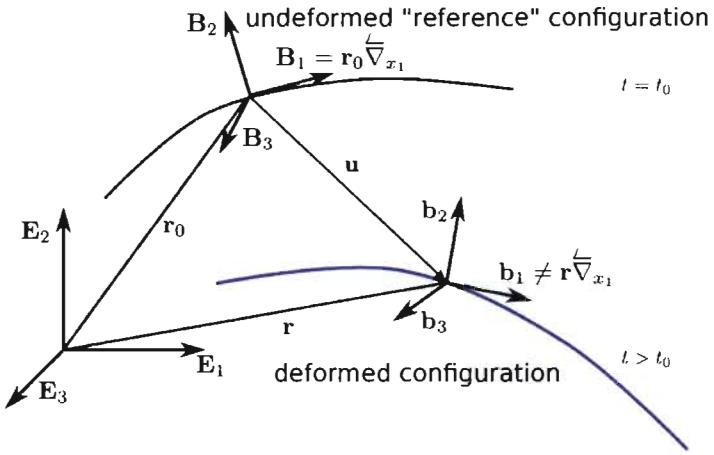

Figure 1. Kinematics of geometrically exact beam theory.

The kinematic description underlying the geometrically exact beam theory is essentially that shown in Figure 1. The green curve in this figure depicts a beam reference axis in its undeformed configuration whilst the blue curve represents the same reference axis in a deformed configuration. Each point along the reference axis is located within the fixed inertial frame, $\mathbf{E}_i$, by the vector, $\mathbf{r}_0$. Associated with each point along the reference axis is a cross section whose orientation is defined by the orthogonal triad of unit vectors $\mathbf{B}_i$. Note that the orientation of $\mathbf{B}_i$ within the fixed inertial frame is defined by the initial sectional rotation tensor, $\mathbf{\Lambda}_0$, i.e., $\mathbf{B}_i = \mathbf{E}_0 \cdot \mathbf{\Lambda}_i$. At some later time, $t > t_0$, the beam reference axis has deformed into a different configuration where each point previously located at $\mathbf{r}_0$ in the undeformed configuration is now located by the vector $\mathbf{r}$ in the inertial frame $\mathbf{E}_i$. In addition, the cross section associated with a particular point along the reference axis has an orientation defined by the orthonormal basis, $\mathbf{b}_i$, which differs from $\mathbf{B}_i$ according to $\mathbf{b}_i = \tilde{\mathbf{B}} \cdot \mathbf{\Lambda}_i$. Here, $\mathbf{\Lambda}_0$ describes initial orientation, $\tilde{\mathbf{\Lambda}}$ is the rotation of a cross-section due to deformation, and $\mathbf{\Lambda}$ is the total rotation aligning the fixed inertial basis, $\mathbf{E}_i$, with the deformed beam cross section axes $\mathbf{b}_i$, i.e., $\mathbf{b}_i = \mathbf{E} \cdot \mathbf{\Lambda}_i$ where $\mathbf{\Lambda} = \tilde{\mathbf{\Lambda}} \cdot \mathbf{\Lambda}_0$.

A key ingredient of the geometrically exact beam theory is that the position of any point in the three-dimensional continuum body (beam in this case) can be expressed as

$$\mathbf{R}_0 = \mathbf{r}_0 + \boldsymbol{\xi}_0 \cdot \mathbf{\Lambda}_0 \tag{1}$$

or

$$\mathbf{R} = \mathbf{r}_0 + \mathbf{u} + \boldsymbol{\xi}_0 \cdot \mathbf{\Lambda} \tag{2}$$

in the undeformed and deformed configurations, respectively, where contributions due to cross-sectional warping are omitted (Cf. Hodges, et al. [19] for a more general representation accounting for warping) and the vector, $\boldsymbol{\xi}_0$, expresses the cross-sectional position $\{0, x_2, x_3\}$ within the reference frame $\mathbf{B}_i$. This enables a continuum displacement field, i.e., $\mathbf{U} = \mathbf{R} - \mathbf{R}_0$ from which classical continuum strain measures can be computed. An important point is that the continuum motion of every point in the three dimensional beam is tracked by a total of

six kinematical parameters, namely, three vector components of the reference axis displacement, $\mathbf{u}$, and three rotation vector parameters, $\boldsymbol{\theta}$, comprising the sectional rotation, $\tilde{\boldsymbol{\Lambda}}(\boldsymbol{\theta})$.

In this paper, isotropic Hooke's law describes the elastic constitutive response such that the continuum stresses, $\boldsymbol{\sigma}$, are related to strains, $\boldsymbol{\varepsilon}$, by $\boldsymbol{\sigma} = \lambda \mathrm{Tr}[\boldsymbol{\varepsilon}]\mathbf{I} + 2\mu\boldsymbol{\varepsilon}$ where μ is the elastic shear modulus and λ the Lamé constant related to Young's modulus, E, and Poisson ratio, ν, as indicated in equation (3), $\mathbf{I}$ is the second order identity tensor, and Tr[*] denotes the trace of *.

$$\mu = \frac{E}{2(1+\nu)} \quad \text{and} \quad \lambda = \frac{\nu E}{(1+\nu)(1-2\nu)} \tag{3}$$

Note, however, that *NLBeam* employs a generally anisotropic Hooke's law suitable for representation of composite cross-sections. The stresses thus obtained allow the strong form of conservation of momentum within the 3D continuum to be expressed as $\nabla \cdot \boldsymbol{\sigma} + \rho \mathbf{f}_b = \rho \ddot{\mathbf{U}}$ where ∇ is the divergence operator, ρ the material mass density per unit volume, $\mathbf{f}_b$ is a body force per unit mass, for example due to gravity, and $\ddot{\mathbf{U}}$ is the acceleration of a given material point. The strong form of the conservation of momentum is integrated across the beam cross-section to get a suitable weak form in terms of generalized sectional forces and strains. Likewise, the local strain energy can be integrated across a cross-section yielding an expression for the strain energy, W, at each point along the beam reference axis in terms of cross-sectional strains, $\boldsymbol{\gamma}$, and curvatures, $\boldsymbol{\kappa}$, i.e.,

$$W = \frac{1}{2}\begin{Bmatrix}\boldsymbol{\gamma}\\ \boldsymbol{\kappa}\end{Bmatrix}^T [\mathbf{C}] \begin{Bmatrix}\boldsymbol{\gamma}\\ \boldsymbol{\kappa}\end{Bmatrix} \tag{4}$$

where the sectional strains and curvatures are computed by

$$\boldsymbol{\gamma} = \boldsymbol{\Lambda}^T \mathbf{r}' - \mathbf{b}_1 \quad \text{and} \quad \boldsymbol{\kappa} = \boldsymbol{\Lambda}^T \boldsymbol{\Lambda}' \tag{5}$$

and ' denotes differentiation with respect to the coordinate along the undeformed beam reference axis, x_1. The components of the sectional strain vector comprise axial strain and transverse shear strains in two directions. The curvature vector comprises the torsional rate of twist about the beam reference axis as well as bending curvature about the other two axes. Differentiating the cross-sectional elastic strain energy of equation (4) with respect to the sectional strains and curvatures yields the sectional forces and moments, respectively, i.e.,

$$\mathbf{F}_N = \frac{\partial W}{\partial \boldsymbol{\gamma}} \quad \text{and} \quad \mathbf{F}_M = \frac{\partial W}{\partial \boldsymbol{\kappa}} \tag{6}$$

For the case of a homogeneous cross-section, as studied in this paper, the cross-sectional elastic matrix is simply, $[\mathbf{C}] = \mathrm{Diag}[EA, GA_2, GA_3, GJ, EI_2, EI_3]$, where Diag indicates a diagonal matrix, A is the area of the cross section, I_2 and I_3 are geometric moments of inertia about the corresponding section axes, J is the polar geometric moment of inertia, and A_2 and A_3 are effective shear areas along the corresponding section axes. Accordingly the sectional forces and moments are simply

$$\begin{aligned} F_{Na} &= EA\,\gamma_1, \quad & F_{Nv2} &= GA_2\,\gamma_2, \quad & F_{Nv3} &= GA_3\,\gamma_3 \\ F_{Mt} &= GJ\,\kappa_1, \quad & F_{Mb2} &= EI_2\,\kappa_2, \quad & F_{Mb3} &= EI_3\,\kappa_3 \end{aligned} \tag{7}$$

where F_{Na}, F_{vi} are the axial and shear forces, respective, and F_{Mt}, F_{Mbi} are the axial torque and bending moments, respective. Equation (7) reflects a linear force-to-strain relationship in the local section coordinate system along the beam; however, the rotation used in transforming into fixed inertial frame is inherently nonlinear (as all rotations are strictly speaking).

The strong form of conservation of momentum is weakened and then implemented into a numerical form (*NLBeam*) using a Petrov-Galerkin finite element discretization in space. The weak form of the equations of motion are expressed as

$$R_I = R_I^m + R_I^d - R_I^e = 0 \tag{8}$$

where the total residual, R_I, at node I, is expressed in terms of contributions from material stress, R_I^m, inertia, R_I^d, and external forces, R_I^e, as computed by

$$R_I^m = \int_0^L \begin{bmatrix} N_I' \mathbf{I} & 0 \\ N_I \mathbf{r}' & N_I' \mathbf{I} \end{bmatrix} \begin{Bmatrix} \mathbf{\Lambda} \cdot \mathbf{F}_N \\ \mathbf{\Lambda} \cdot \mathbf{F}_M \end{Bmatrix} dx_1$$

$$R_I^d = \int_0^L N_I(x_1) \begin{Bmatrix} \rho A \ddot{u} \\ \dot{\mathbf{W}} \mathbf{J}_\rho \mathbf{W} + \mathbf{J}_\rho \mathbf{A} \end{Bmatrix} dx_1 \tag{9}$$

$$R_I^e = \int_0^L \begin{Bmatrix} N_I \rho A \mathbf{f}_b \\ 0 \end{Bmatrix} dx + \sum_k N_I(x_1^k) \sum \begin{bmatrix} \mathbf{\Lambda} \cdot \bar{\mathbf{f}}_k \\ \mathbf{\Lambda} \cdot \bar{\mathbf{m}}_k \end{bmatrix}$$

In equation (9), $\mathbf{W}$ and $\mathbf{A}$ are the angular velocity and acceleration, respectively, of a point on the beam reference axis, $\mathbf{J}_\rho$ is the cross-sectional inertia tensor (a cross-sectional property), and $\bar{\mathbf{f}}$ and $\bar{\mathbf{m}}$ are concentrated forces and moments, respectively. Additionally, the elemental shape functions, N_I, have been introduced and are quadratic Lagrange interpolating polynomials in *NLBeam*, thus each element comprises three nodes. Integration of these terms is carried out using (reduced) two point Gauss quadrature over the length of each element. Equation 8 reflects a nonlinear system of equations whose independent variables are the incremental nodal degrees of freedom, $\Delta\mathbf{u}$ and $\Delta\boldsymbol{\theta}$, and is solved using a Newton-Raphson iterative scheme.

3. Experimental Approach

Toward the overarching research goal, experimental procedures were performed with the role of providing data for comparison to numerical results from *NLBeam* simulations. It was intended that surrogate beams be driven into large, i.e., nonlinear, deformation. The experimental effort consisted of imposing base excitations on three blades of differing geometry in three different orientations under varying excitation amplitudes in order to create and observe the desired nonlinearities.

To accomplish the experimental goal of driving and identifying geometrically nonlinear deformation, specific test specimens were designed with differing geometries. Each geometry consists of a different tapered width profile and a constant thickness of 0.32 cm selected for practical reasons during fabrication, as seen in Figure 2. These width profiles were selected in order to evaluate *NLBeam's* modeling capabilities for nonprismatic beams, a purely geometric consideration. To minimize experimental variability and model uncertainty the specimens were fabricated of Aluminum 6061. Although typical wind turbine blades are made of optimized fiber reinforced composite lay-ups, aluminum was chosen due to its well-documented homogenous, isotropic material properties.

The physical experimental setup consists of a surrogate blade specimen fixed to a base, replicating a fixed-free cantilever beam which is fairly representative of operating turbine-blade boundary conditions. The base is then bolted to a VTS Model VG 100-6 shaker, suitable for driving the desired base excitations. Each specimen was excited in the flap-wise bending direction in three different orientations, viz. horizontal-flat, horizontal-edge, vertical, as seen in Figure 3, to explore geometric nonlinearities due to differing gravitational loads. This is a relevant response condition because wind turbine blades experience changing stress fields which are attributed to varying gravitational loading throughout their rotations. A small mass of approximately 50g was attached to the end of each surrogate blade as seen in Figure 4. The mass served to exaggerate geometric nonlinearities observed in the experimental procedures; however, the additional inertial forces induced rocking motion of the base. This rocking complicated the boundary conditions input to the model.

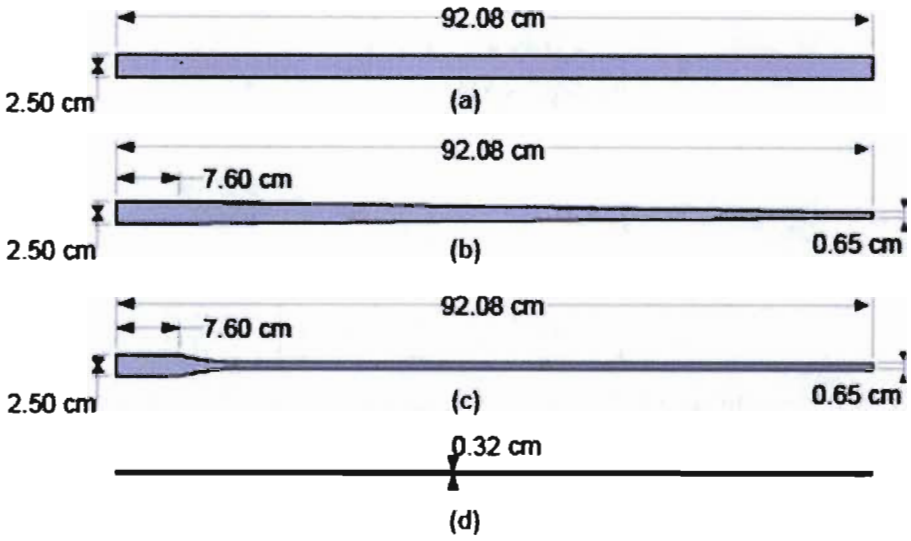

Figure 2. Geometry of the surrogate blade test specimen used in experiments; **(a)** non-tapered, **(b)** linear taper, **(c)** radiused taper, **(d)** uniform thickness profile for all geometries.

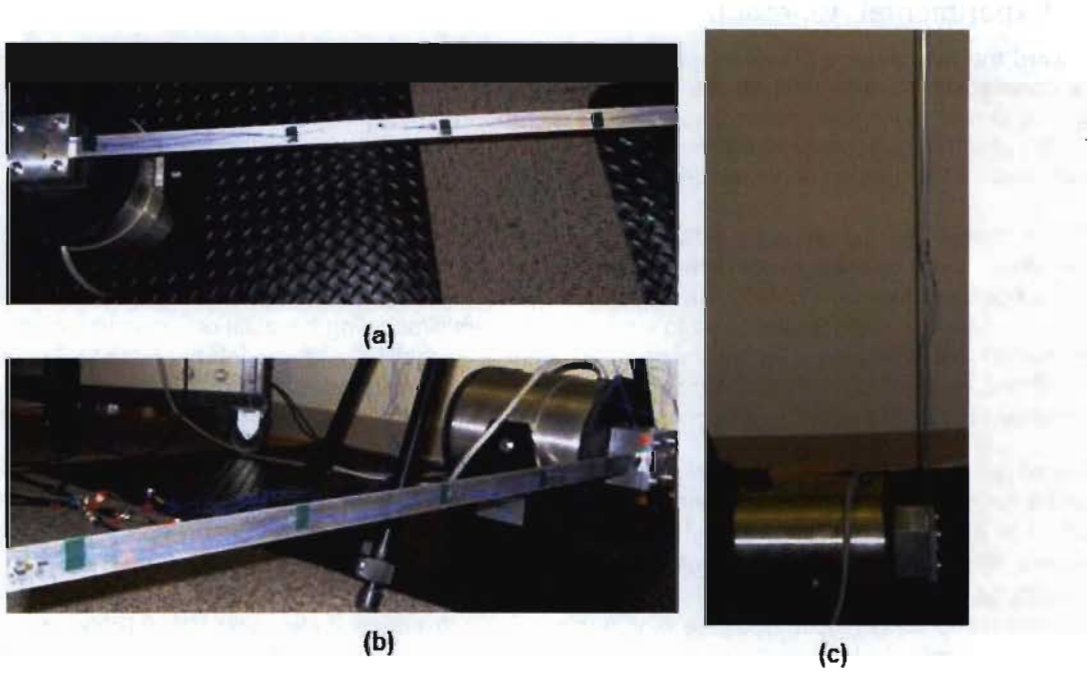

Figure 3. Three blade orientations investigated; **(a)** horizontal flat **(b)** horizontal edge **(c)** vertical.

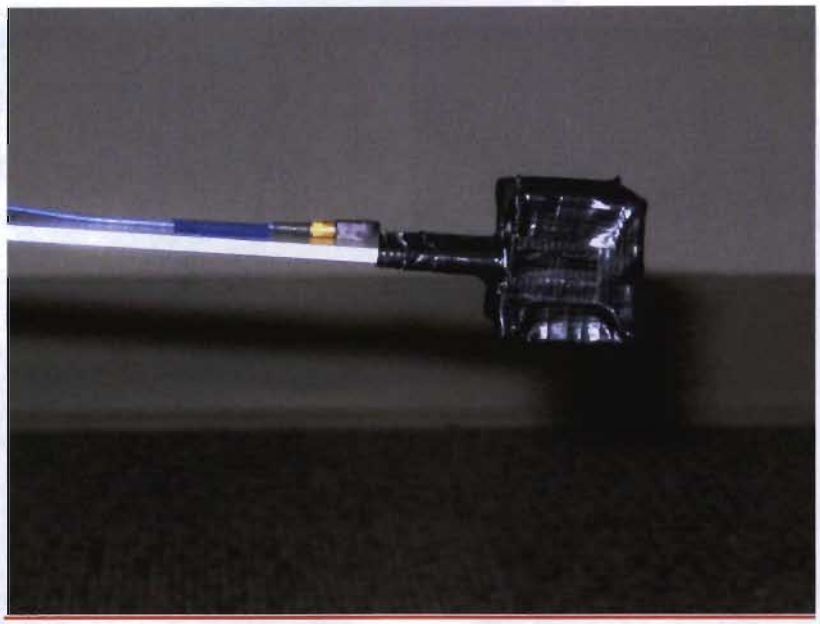

Figure 4. Mass attached at tip to help drive geometrically nonlinear deformation.

Excitation signals used to dynamically drive the system originate from a *Dactron* data acquisition system which sends the desired excitation voltage through a power amplifier and, ultimately, to the shaker which drives the surrogate blade. Excitation signals used comprise of (i) random and (ii) sine dwell. *Dactron* configurations for each excitation are shown below in Table 1. Random base excitations were used to generate a comprehensive baseline frequency response function (FRF) to identify natural frequencies and screen for nonlinear responses. Sine dwells were then utilized to focus on specific frequencies for generating data that could easily be compared to simulation results. Sine dwell excitation was advantageous to this research in that the degree of nonlinearity of response data can be easily measured using a harmonic distortion metric, represented in Equation (10), where a_n represents the magnitude of the response at the n^{th} harmonic. A large value for this metric implies a highly nonlinear system.

$$H_D = \frac{1}{a_1}\sqrt{\sum_n a_n^2} \tag{10}$$

Because the Dactron system restricts the total number of data input channels to four, careful channel allocation and sensor placement was important. To aid in this task, a solid/continuum finite element model of one blade geometry was developed to estimate representative modal characteristics using the commercial finite element software, *Abaqus*. The preliminary mode shapes were used to aid sensor placement on the test specimens and also provide some frame of reference for specifying excitation signal parameters. Two accelerometers were placed on the base fixture, one on the back end and one on the front end in order to capture any base rocking, one accelerometer is placed approximately at the midspan of the beam, and one accelerometer is placed near the beam's tip, as seen in Figure 5. Early experiments collected base displacement data from a laser vibrometer (as shown in Figure 5), but this approach was aborted because (i) it could not capture the rotation of the base and (ii) the data contained prohibitive levels of noise for use as boundary conditions for input to a numerical model.

Table 1. Dactron settings for each excitation type

	Cutoff Frequency	Data Points	Spectral Lines	Other
Random	250	4096	1600	0.5 Vrms
On-Resonance Sine	500	4096	1600	57 Hz
Off-Resonance Sine	250	4096	1600	35 Hz

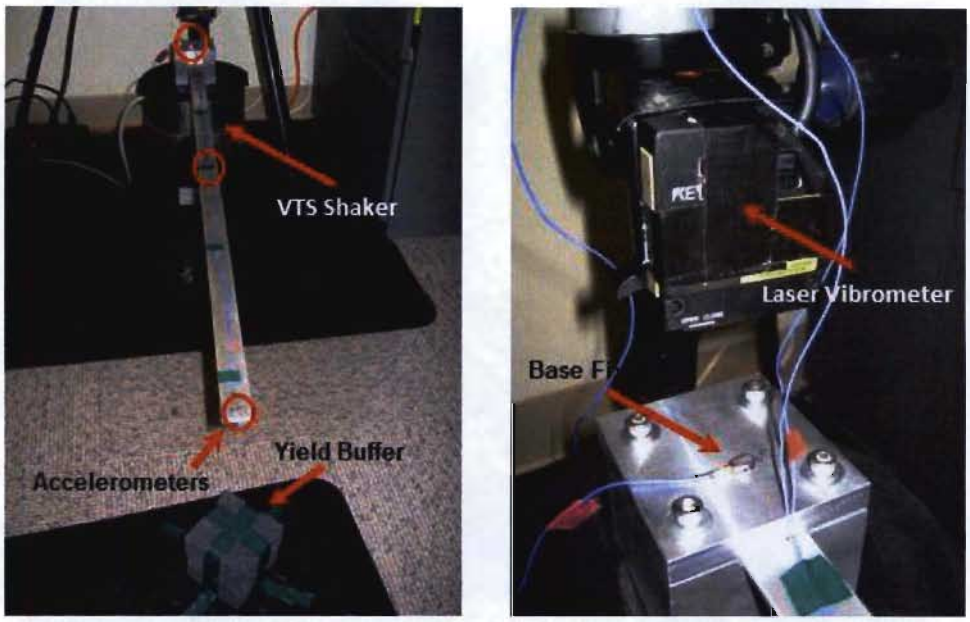

Figure 5. Experimental setup.

4. Numerical Modeling

Toward the goal of establishing the predictive capability of *NLBeam* and highlighting nonlinear structural dynamic response when present, two different FE modeling approaches were utilized to simulate the experiments. The two modeling approaches used were (i) a geometrically nonlinear model using *NLBeam* and (ii) a linear modal superposition model using the commercial FE modeling package *Abaqus*. The role of the nonlinear model is to demonstrate acceptable agreement between *NLBeam* and experimental results, while the use of a linear model aims to highlight geometric nonlinearities in observed response. In both cases, simulation output results are directly compared with experimental data to substantiate quantitative and qualitative assessments.

To model surrogate blades, *NLBeam* uses quadratic beam elements based on the geometrically exact beam theory as described above. Each node includes six degrees of freedom (DOF); three translations and three rotations in (and about, respectively) the global x, y, and z directions. At each elemental integration point along the length of the beam, two-dimensional cross-sectional properties, shown in Table 2, are defined via a sectional properties pre-processor developed as part of this work.

The linear superposition model employs the *Abaqus* beam element, *B32*, which is a quadratic beam element in space, also accounting for six degrees of freedom at each node. Rectangular beam cross-section properties are calculated directly within *Abaqus* from sectional widths and thicknesses corresponding to the center node of each element given as input. The response data from the modal superposition model reflects a superposition of the first four modal responses accounting for each mode's participation factor.

Boundary condition input data (displacement/acceleration time histories) for both models were generated from base accelerometer data measured in experiments. *NLBeam* is limited to accept only displacement (rather than acceleration) time histories as boundary conditions; therefore the measured experimental acceleration data was converted into suitable displacement data. Rocking (rotation about global z-axis) of the base, attributed to the addition of a tip mass, was observed in experimental data. This feature of the boundary conditions was significant enough that it was necessarily accounted for in a manner ensuring both the translational and rotational base accelerations were preserved.

Table 2. Material and sectional property relations used in pre-processor.

Parameter	Symbol	Value
Young's Modulus	E	69 GPa
Shear Modulus	G	26 GPa
Density	ρ	2.70 g/cm^3
Area	A	w*h
Torsion Constant	J	$hw^3\left(\frac{1}{3}-0.21\frac{w}{h}\left(1-\frac{w^4}{12h^4}\right)\right)$
Moments of Inertia (y-dir)	I_y	$\frac{wh^3}{12}$
Moments of Inertia (z-dir)	I_z	$\frac{hw^3}{12}$

To achieve this, assumed rigid body translational and angular acceleration are computed from both accelerometers on the base according to Equation (11), where a_b is translational acceleration, α_b is rotational acceleration, and a_1, a_2 are the measured accelerations from two sensors on the assumedly rigid base.

$$a_b = \frac{a_1 + a_2}{2} \quad \alpha_b = \frac{a_1 + a_2}{r_{12}} \tag{11}$$

These rigid body accelerations were high-pass filtered, H_h, and doubly integrated to obtain displacement and rotation data, i.e.,

$$u_b = \iint H_h(a_b)dt \quad \theta_b = \iint H_h(\alpha_b)dt \tag{12}$$

Finally, pure translational displacements applicable to nodes on the base are calculated according to Equation (13) and low pass filtered, H_l, to reduce high frequency noise. The key reason for calculating displacement in this manner is to preserve relative phase information between translational displacement and angular rotation that is essential for parity of simulations and experiment.

$$u_1 = H_l\left(u_b + \frac{r_{12}}{2} * \theta_b\right) \; u_2 = H_l\left(u_b - \frac{r_{12}}{2} * \theta_b\right) \tag{13}$$

The result of this scheme is highlighted in Figure 6 where a representative measured experimental acceleration time history is compared with the acceleration time history as computed by *NLBeam* given the displacement input boundary conditions. It is clear from this figure that the angular and translational motion including the relative phase is preserved.

The nominal *NLBeam* model consisted of 24 elements, of which, one element corresponded to the relatively rigid base holding the surrogate blade. This element was effectively stiffened to reflect the rigid body motion of the base fixture. The base displacement input time history computed according to Equation (13) was specified as nodal boundary conditions for the first and last node of this "fixture-base-beam" element. A point mass was included at the tip node corresponding to the experimental tip mass. Simulation results from the *NLBeam* model used for comparison to experiment in this paper come from a node located 86 cm from the base of the blade corresponding to the location of tip accelerometer. As suggested by Equation (9), *NLBeam* directly includes contributions from gravitational forces as well as the nonlinear geometric stiffening due to stresses in the beam. Accordingly, simulations were conducted using the *NLBeam* model for all three surrogate blade geometries across all three orientations to compare to assess the influence of the orientation with respect to gravity.

Much consideration was given to ensuring that parameters and boundary conditions for the modal superposition model, utilizing *Abaqus,* were as close to those employed in *NLBeam* as the software would allow, in order for meaningful comparisons. Thus, the nominal modal superposition model consisted of 23 elements with one element allocated to the base fixture of the experimental setup. Similar to the *NLBeam* case, this element was

stiffened in order to ensure the assumed rigid body motion boundary condition; however, since acceleration time histories can be specified directly as boundary conditions within this FE code, base accelerometer data measured in experiments were used as excitation sources for te linear superposition model. Likewise, a point mass corresponding to the mass used in experimentation was applied to the final node in the model. All data extracted from the modal superposition model and presented herein are from a node located 86 cm from the base of the blade which corresponds to the location of the tip accelerometer. The surrogate's response across all three orientations was simulated using a gravitational preload in an effort to explore the effects of gravity on a linear (perturbation) model.

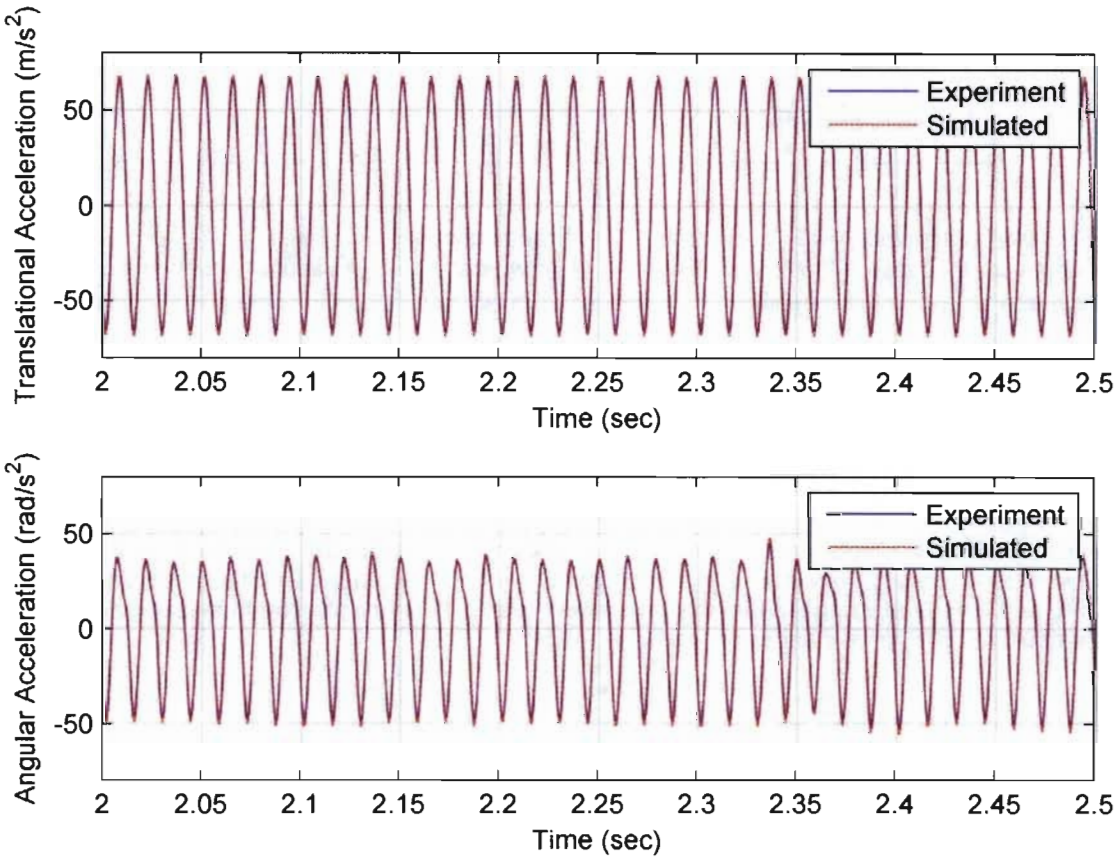

Figure 6. Comparison of translational **(top)** and rotational **(bottom)** acceleration at the base between *NLBeam* and experiment

5. Results and Discussion

Ultimately, it is desired to experimentally validate *NLBeam* over a range of response regimes including behavior that exhibits varying levels of geometric nonlinearity. Achieving such conditions in this study proved to be difficult with the available experimental hardware and code capabilities. Physical restraint of the shaker system was difficult under cases of large deformations because of the large accelerations and resulting base moments associated with such motion. The base moments also induced the aforementioned rotations (rocking) of the base of the blade where it affixes to the shaker. Furthermore, the shaker itself has internal physical stops which limited the amplitude of base displacement. In light of these experimental limitations, the most efficient manner to drive large deformations was to operate the shaker near a resonant frequency of the beam. However, simulating this behavior near resonance was complicated because the model did not directly include physical damping.

Accordingly, this section compares simulation and experiment results for near resonance and off resonance cases and, perhaps more importantly, discusses improvements in both experiment and model that can be used in the future.

5.1. Fixture base rotation complexities

As was discussed previously, a mass of approximately 50g was added to the tip of the surrogate blades to enhance any nonlinearity in the response of the test specimen. The addition of this mass increases the inertial loading, in turn, causing the "rocking" motion of the base. This rocking is not driven by the shaker, *per se*, but is permitted due to the compliance of that system. The kinematic motion of this rocking behavior is captured and input as boundary conditions to the model as discussed in Sections 3 and 4. Figure 7 shows a representative normalized power spectral density (PSD) of an experimental case prior to and following the addition of the 50g mass. The tip acceleration of the surrogate blade with tip mass contains several harmonics of the fundamental excitation frequency (57 Hz in this case), whereas the signal from the case without a tip mass does not. Presumably this difference is a manifestation of nonlinearity in the system response which is enhanced by adding the mass.

However, the source of nonlinearity in this experimental configuration cannot be isolated to the surrogate blade response and it is believed to be attributable, as least in part, to a nonlinear interaction between the shaker and the test specimen. This coupling cannot be directly accounted for in the simulations because they model the surrogate blade only, i.e., there is not a direct model of the shaker system or its interface with the surrogate beam. With the objective of model validation this is viewed as a limitation of the experiment (in permitting such induced rotations) rather than the model, as there is no desire to develop a physical model of the shaker system.

It is interesting that the induced rocking behavior is characteristic of a bi-stable phase orientation between the rigid base translation and base rotation. Figure 8 illustrates this behavior as follows. A representative experimental case (non-tapered beam, horizontal-flat orientation, with a normalized input amplitude of 2.0 at 57 Hz), was repeated ten times. The acceleration time histories measured by two accelerometers located on the shaker base fixture are plotted in Figure 8. The rear-most accelerometer data appears relatively repeatable and is plotted in blue with sinusoidal amplitude of approximately 4 m/s^2. Data from the forward-most accelerometer separates into two distinct categories of response classified by their respective amplitudes, i.e., approximately 2 and 6 m/s^2. This indicates a base rotation that falls into one of two bistable operational modes; one is in phase with the base translation and contributes additively to the forward-most accelerometer and the other mode is 180 degrees out of phase with the base translation, thus contributing subtractively to the forward-most accelerometer.

As suggested in Section 3, one measure of system nonlinearity is the harmonic distortion of an output signal observed when the system's input is a pure sinusoid at a single frequency. The relevance of this metric is revealed by considering that a nonlinear model, M, relating inputs, x, to outputs, y, can be expressed in a power series. If x is a pure sinusoid then harmonics of the frequency of x appear in the output

$$Y = M(X) = \sum_{n=0}^{\infty} M_n (X - C)^n \tag{14}$$

If, for the sake of discussion, $X = a\sin(\omega t) + b\cos(\omega t)$, then Equation (14) yields a Fourier series, i.e.,

$$Y = A_0 + \sum_{n=0}^{\infty} A_n \sin(n\omega t) + B_n \cos(n\omega t) \tag{15}$$

where a, b, A_i, B_j, are constants pertaining to the model and input data, n is an integer specifying each harmonic of the original signal input frequency, ω. Clearly, if the system is nonlinear, then the output will contain harmonics of the original input frequency. Figure 9 presents the harmonic distortion computed from measured tip acceleration collected from experiments conducted at each orientation for the prismatic beam versus a normalized magnitude of the input excitation amplitude. The harmonic distortion increases with the input amplitude up to a maximum value that is unique for each case. Further increases in input amplitude result in a decrease in the observed nonlinearity. The source of this behavior is unclear, but we speculate that such experimental nonlinearity is caused by the mechanical connection between the surrogate blade and the shaker

fixture. This type of behavior is consistent with a stick-slip transition in this mechanical connection where nonlinearity is most profound near the incipient transition from stick to slip response. At low amplitudes the connection behaves essentially linearly, at increasing amplitudes up to some point the connection spends more time near the stick-slip transition. However, as amplitudes continue to increase the response is dominated by the slip condition manifest as frictional dissipation (itself a nonlinearity, though perhaps not as profound as the transition.) The experiments generating this data were conducted in turn at each orientation in the order: (1) flat-horizontal, (2) edge-horizontal, (3) vertical. Immediately after completing the experiment in the vertical orientation, the experiment was repeated under the flat-horizontal orientation. Results from this final case are plotted in green in Figure 9 and clearly differ from the original experiment conducted in this orientation (shown in blue). The lack of agreement between this data and that from the initial flat-horizontal case indicates a change in the system throughout the progression of these experiments. This change is consistent with the theory of the stick-slip transition nonlinearity. Such behavior would probably be influenced by the specific details of the interface between the surrogate blade and base fixture. The apparatus was disassembled and reassembled between each experimental case, accordingly, such connection details, for example bolt preload, are most likely different between each case. No attempt was made to characterize or control these connection details.

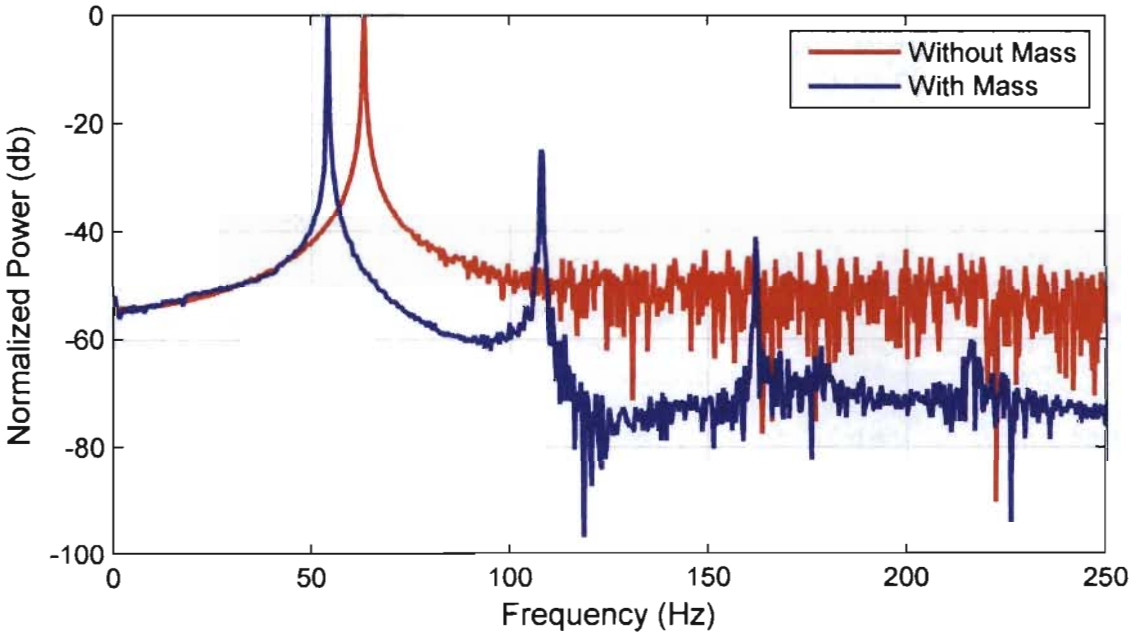

Figure 7. PSD of tip acceleration without mass (**red**) and with mass (**blue**).

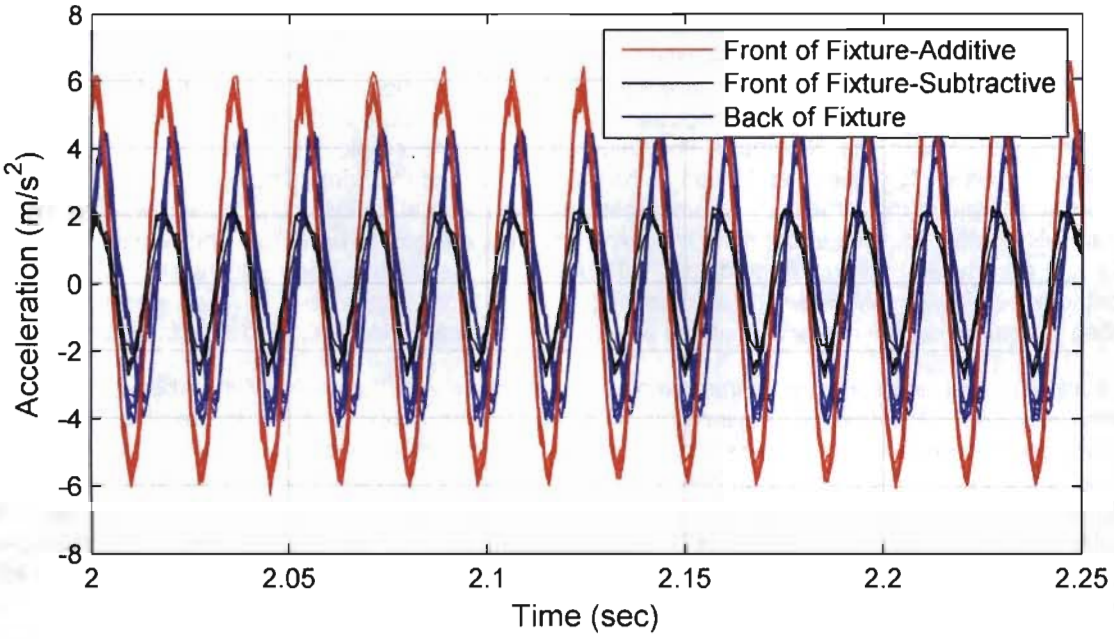

Figure 8. Representative measured acceleration time histories from multiple experimental repeats. Data from accelerometer on rear of fixture is plotted in **blue**. Data from accelerometer near the front of base fixture separates into two distinct phases of base rotation: additive (**plotted in red**) and subtractive (**plotted in black**).

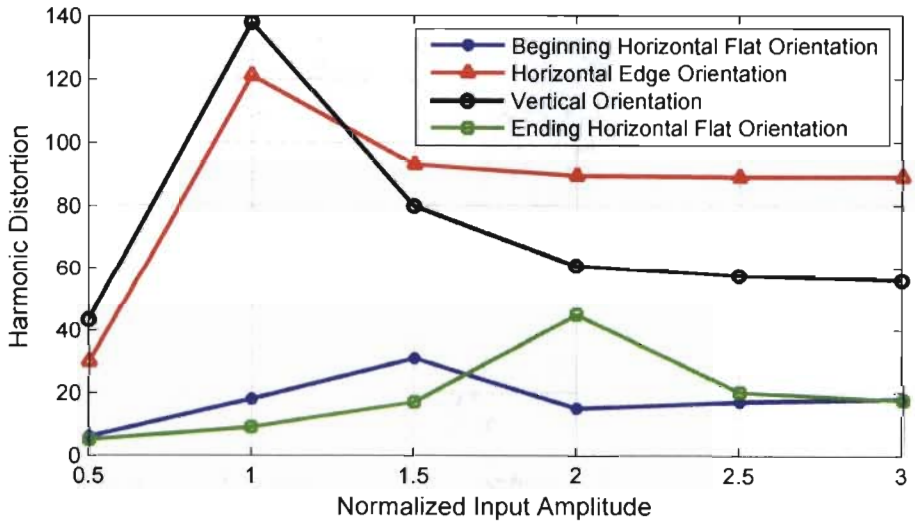

Figure 9. Harmonic distortion of measured tip acceleration response versus input amplitude (normalized) for various orientations of surrogate blade.

5.2. On-Resonance Results

Predicting response under sine-dwell excitation at a frequency near resonance is complicated because of the base rocking complexities previously discussed as well as the lack of physical damping in *NLBeam*. The first issue is addressed to a limited extent by specifying a rotational motion of the base in the finite element models that coincides with the observed rocking accelerations. The latter issue is handled to some extent by numerical damping associated with the Newmark time integration scheme employed by *NLBeam*. Physical damping mechanisms in this system comprise friction at the fixture base and material damping in the beam. *NLBeam* was developed to represent the structural dynamic response within an aeroelastically coupled wind turbine modeling code. In this context the actual damping mechanisms are expected to be dominated by interaction of relative velocity and aerodynamic drag. Accordingly, little attention thus far has been devoted to modeling material or frictional damping within *NLBeam*. One consequence is poor agreement (over predicting amplitudes) in predicting structural response near resonance where the numerical model is unstable for truly zero damping.

Aside from damping, another issue is the complexity associated with the shaker-fixture-beam interface, which is not being modeled. It is unclear precisely the influence of this coupling, but it is possible that represent the nonlinearly coupled behavior by simply specifying base rotations, while conceptually sounds, overly constrains the response of the model. Also, it is important to note that the tip accelerometer is essentially near a node of the operational deflected shape point, thus the acceleration reported at this point is presumably sensitive to details such as the precise location of the sensor/FE-node. Attributing the discrepancy between model and experiment to these issues is somewhat speculative; however, it is recommended that the experimental program be adjusted to eliminate these uncertainties.

Figure 10 presents a representative comparison between experimentally observed and *NLBeam* prediction of tip acceleration for surrogate blade without taper in the horizontal-flat orientation. The general response is captured by *NLBeam*, albeit with a significantly subdued amplitude for this particular period of the total time history. Other orientations and surrogate geometries are not discussed here because of the issues described previously.

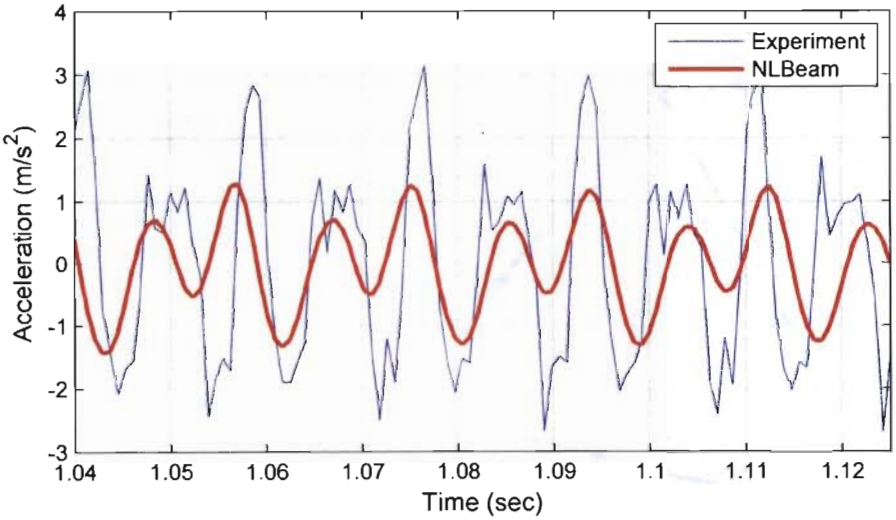

Figure 10. Comparison of tip acceleration time history for horizontal-flat orientation excited with sine dwell near resonance (57Hz).

5.3. Off-Resonance Results

In order to eliminate many of the issues discussed in the previous sections, an off-resonance low-amplitude set of experiments was also conducted. Results from these tests enable a more meaningful (and consequently, better quantitative) comparison between experiment and models. On the other hand, the very nature of these experiments restricts comparisons to a fundamentally linear regime of response. For example, consider Table 3, which reports the harmonic distortion of the experimentally measured tip acceleration for the surrogate blade with no taper in a horizontal flat orientation for near- (57Hz) and off- (35Hz) resonance cases. Clearly, there is no significant nonlinearity present in the response for this case.

Table 3. Experimental harmonic distortion for tip acceleration response for no taper, horizontal flat orientation.

Orientation	Sine at 35 Hz	Sine at 57 Hz (third mode)
Horizontal Flat	1.00	26.48
Horizontal Edge	1.00	8.42
Vertical	1.00	6.72

In order to make some comparison, a frequency domain correlation metric is defined as

$$C_{12} = \frac{A_1(\omega) \cdot A_2(\omega)}{\|A_1(\omega)\| \, \|A_2(\omega)\|} \tag{16}$$

where $A_i(\omega)$ is the acceleration response in the frequency domain for the i^{th} signal and the inner product is taken over the frequency domain. This particular correlation metric is used because it measures how well the shape of the two signals match in the frequency domain, although it does not strongly penalize discrepancy in the magnitudes of those signals. Computed values of this correlation metric between experimental data and each of the two modeling approaches are shown in Table 4. Generally, both modeling approaches do well, although they tend to perform better predicting response in a horizontal–edge orientation. As expected, the modal superposition and geometrically nonlinear model are highly correlated in the frequency domain. Thus, the geometrically nonlinear approach offers negligible advantage for modeling dynamic response dominated by linear behavior. Comparisons of acceleration time histories shown in Figure 11 Figure 13 affirm this conclusion; although, in some cases *NLBeam* compares more favorably than the model superposition results. Such "eyeball" comparisons can be misleading and development of a quantitative metric for comparing nuances of time history data is recommended for future work. Note in particular, acceleration time histories for both models compare reasonably with experiment for the non-tapered beam (Cf. Figure 11-Figure 13). On the other hand, neither model does well matching experimental response for the linear tapered beam as shown in Figure 14. A possible source of error is that the relatively coarse mesh cannot adequately capture the varying geometry. While a thorough grid convergence study has not been performed to assess the accuracy of the results for the linear taper case, it is expected that is not the sole source of discrepancy between the experiment and model and more work needs to be done to rectify this case. Finally, results for the radiused taper case are presented in Figure 15. In this case, *NLBeam* appears to capture the experimental response with better agreement than modal superposition.

Table 4. Computed frequency domain response correlation metric values.

	NO TAPER			LINEAR TAPER			RADIUSED TAPER		
	Flat	Edge	Vert	Flat	Edge	Vert	Flat	Edge	Vert
Exp.- NLB	0.985	0.985	0.977	0.977	0.981	0.952	0.979	0.982	0.975
Exp.- ABQ	0.984	0.982	0.974	0.978	0.982	0.956	0.982	0.984	0.976
ABQ - NLB	0.995	0.992	0.996	0.998	0.998	0.993	0.995	0.994	0.992

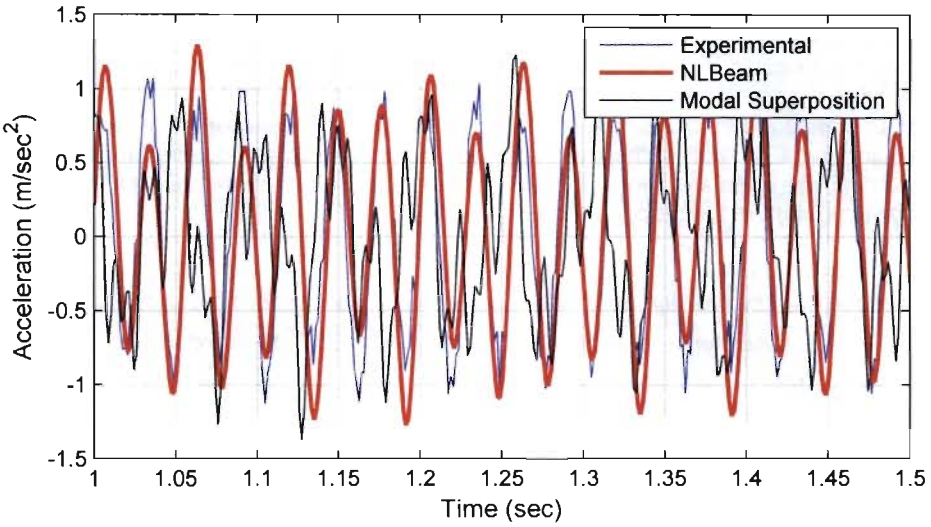

Figure 11. Comparison of tip acceleration response for no taper and horizontal-flat orientation

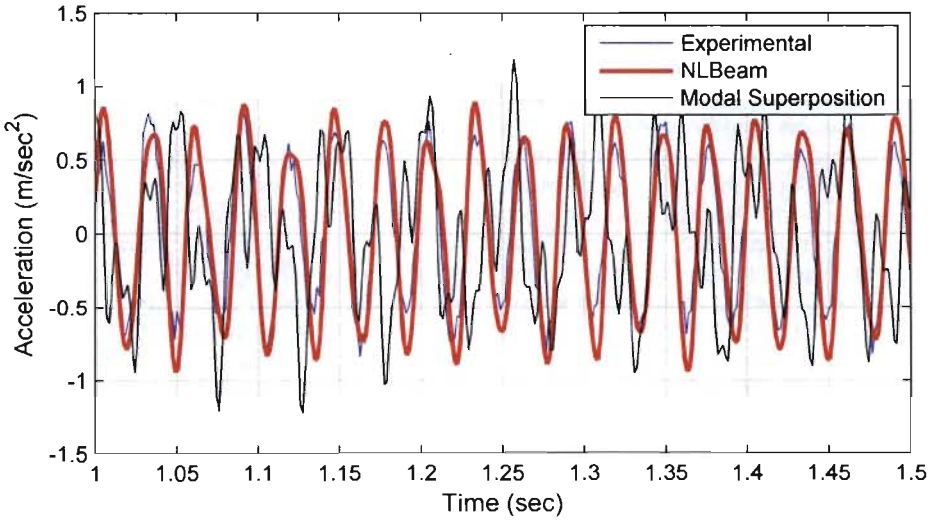

Figure 12. Comparison of tip acceleration response for no taper and horizontal-edge orientation.

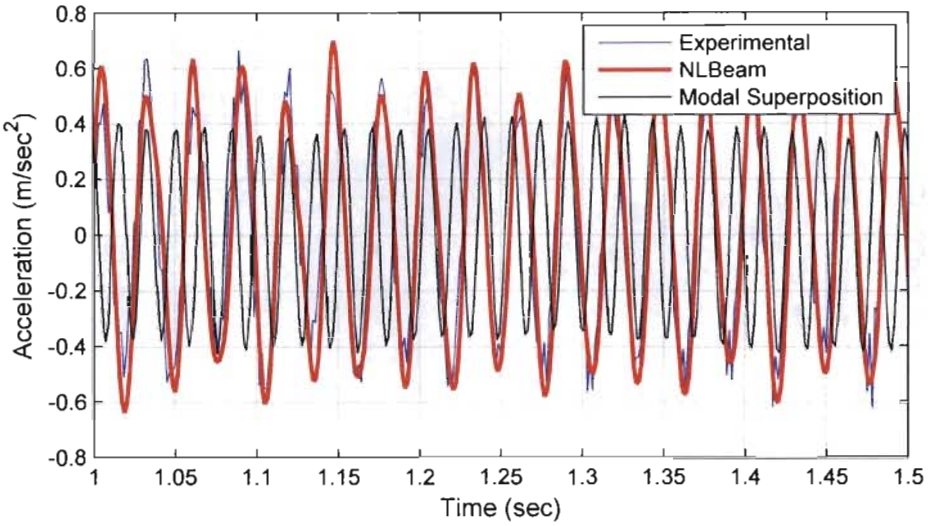

Figure 13. Comparison of tip acceleration response for no taper and vertical orientation.

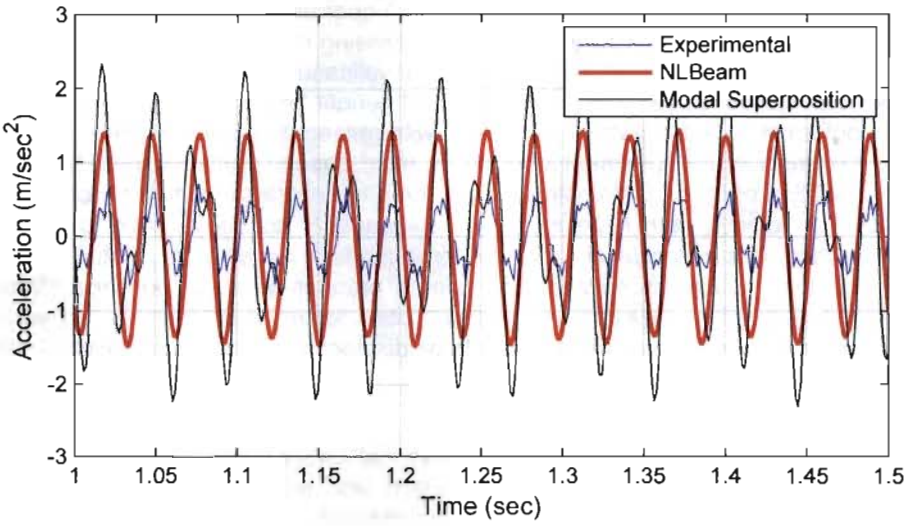

Figure 14. Comparison of tip acceleration response for linear taper and horizontal-flat orientation.

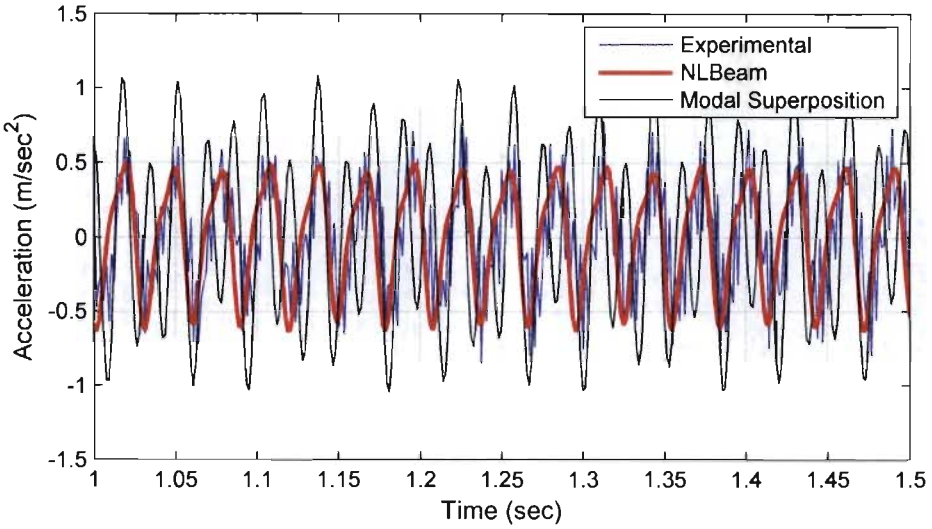

Figure 15. Comparison of tip acceleration response for radius taper and horizontal-flat orientation.

6. Conclusions

This paper presents work conducted within the scope of the 2011 Los Alamos Dynamics Summer School. The intention was to develop an experimental program supporting validation of a geometrically nonlinear structural dynamics code under development as part of Los Alamos National Laboratory's effort to expand modeling capabilities for wind turbines amenable to simulation of entire operating plants. The experimental technique and modeling presented in this paper are directly capable of assessing the influence of orientation of laboratory-size surrogate blades under small base excitation. Experimental validation of simulation capabilities under conditions of truly large deformation response remains elusive, but will benefit from the findings reported in this paper. For conditions of small deformation and varying orientations with respect to gravity, simulation results from the code *NLBeam* compare favorably with experimental results in most cases. Future capability enhancements to this code consist of the addition of physical damping mechanisms to enable simulation of response near resonance, allowing specification of rotation time histories as nodal boundary conditions, and providing for the input of accelerations rather than displacement or rotation for boundary conditions. Future improvements to the experimental program that would enable validation over a broader range of nonlinear deformation response include the addition of sensors to measure the resultant base forces and moments, an actuation system that eliminates inadvertent base rotations and that permits large displacement and acceleration amplitudes.

Acknowledgements

The authors would like to acknowledge Los Alamos National Laboratory's Engineering Institute (Dr. Charles Farrar, Director) for providing the funding to perform this research, as well as Vibrant Technologies and Simulia for their kind donation of software, *MEScope* and *Abaqus,* respectively, which was integral in the completion of this study. DJL wishes to acknowledge the financial support of LANL's Intelligent Wind Turbine Lab Directed Research and Development program (Dr. Curtt Ammerman, PI).

References Cited

[1] U.S. Department of Energy (2008). "20% Wind Energy by 2030."
[2] U.S. Department of Energy (2010). "HIGRAD/Windblade Wind Generation Modeling and Simulation."
[3] Walford, C.A. (2006) "Wind Turbine Reliability: Understanding and Minimizing Wind Turbine Operation and Maintenance Costs" Sandia Report. SAND2006-1100
[4] Robinson, M.C., Luttges, M.W., Miller, M.S., Shipley, D.E. and Young, T.S. (1994) "Wind Turbine Blade Aerodynamics: The Analysis of Field Test Data," National Renewable Energy Lab. NREL/TP-441-7108 CONF-940113-11

[5] National Wind Technology Center (2010) "Wind Energy Aerodynamics/Aeroacoustics," National Renewable Energy Laboratory. NREL/FS-5000-48830.
[6] Jonkman, J. M. and Buhl Jr., M. L. (2005), "FAST User's Guide," NREL/EL-500-29798. Golden, Colorado: National Renewable Energy Laboratory.
[7] Jonkman, J.M., NWTC Design Codes http://wind.nrel.gov/designcodes/simulators/fast/ . Last modified 05-November-2010; accessed 20-June-2011.
[8] Kane, T.R. and Wang, C.F. (1965) "On the Derivation of Equations of Motion," *Journal of the Society for Industrial and Applied Mathematics.* Vol. 13, No.2, pp. 478-492.
[9] Kane, T.R. and Levinson, D.A. (1997) *Dynamics: Theory and Applications.* MacGraw-Hill Series in Mechanical Engineering. MacGraw-Hill Book Company, New York.
[10] Bazilevs, Y., Hsu, M.C., Akkerman, I., Wright, S., Takizawa, K., Henicke, B., Spielman, T., and Tezduyar, T.E. (2011) "3D Simulation of Wind Turbine Rotors at Full Scale. Part I: Geometry Modeling and Aerodynamics," *International Journal of Numerical Methods in Fluids,* Vol. 65, pp. 207-235.
[11] Bazilevs, Y., Hsu, M.C., Kiendl, J., Wuchner, R., Bletzinger, K.U. (2011) "3D Simulation of Wind Turbine Rotors at Full Scale. Part II: Fluid-structure Interaction Modeling with Composite Blades," *International Journal of Numerical Methods in Fluids,* Vol. 65, pp. 236-253.
[12] Zhang, J.P, Pan, L.L, Three-dimensional modeling and aeroelastic coupling analysis for the wind turbine blade, *WNWEC 2009 - 2009 World Non-Grid-Connected Wind Power and Energy Conference*, Nanjing, China, September 2009.
[13] Reissner, E. (1972) "On One-Dimensional Finite-Strain Beam Theory: The Plane Problem," *Journal of Applied Mathematics and Physics,* Vol 32, pp. 795-804.
[14] Reissner, E. (1981) "On Finite Deformations of Space-Curved Beams," *Journal of Applied Mathematics and Physics,* Vol. 32, pp. 7334-744.
[15] Simo, J.C. (1985) "A Finite Strain Beam Formulation. The Three-dimensional Dynamic Problem, Part I," *Computer Methods in Applied Mechanics and Engineering,* Vol. 58, pp. 55-70.
[16] Simo, J.C. and Vu-Quoc, L. (1986) Á Three-dimensional Finite-Strain Rod Model. Part II: Computational Aspects," *Computer Methods in Applied Mechanics and Engineering,* Vol. 58, pp. 79-116.
[17] Jelenic, G. and Crisfield, M.A. (1999) "Geometrically Exact 3D Beam Theory: Implementation of a Strain-Invariant Finite Element for Statics and Dynamics," *Computer Methods in Applied Mechanics and Engineering*, Vol. 171, pp. 141-171.
[18] Bauchau, O.A. (2011) *Flexible Multibody Dynamics.* Solid Mechanics and Its Applications. Vol. 176, New York: Springer.
[19] Hodges, D.H. and Yu, W. (2006) A Rigorous, Engineer-friendly Approach for Modeling Realistic Composite Rotor Blades, *Wind Energy,* Vol. 10, pp. 179-193.